Laser-directed hierarchical assembly of liquid crystal defects and control of optical phase singularities

Paul J. Ackerman[1,2], Zhiyuan Qi[1], Yiheng Lin[1], Christopher W. Twombly[1], Mauricio J. Laviada[1], Yves Lansac[1,3] & Ivan I. Smalyukh[1,2,4,5]

[1]Department of Physics and Liquid Crystal Materials Research Center, University of Colorado, Boulder, Colorado 80309, USA, [2]Department of Electrical, Computer, and Energy Engineering, University of Colorado, Boulder, Colorado 80309, USA, [3]GREMAN, Université François Rabelais-CNRS, UMR 7347, 37200 Tours, France, [4]Materials Science and Engineering Program, University of Colorado, Boulder, Colorado 80309, USA, [5]Renewable and Sustainable Energy Institute, National Renewable Energy Laboratory and University of Colorado, Boulder, Colorado 80309, USA.

Topological defect lines are ubiquitous and important in a wide variety of fascinating phenomena and theories in many fields ranging from materials science to early-universe cosmology, and to engineering of laser beams. However, they are typically hard to control in a reliable manner. Here we describe facile erasable "optical drawing" of self-assembled defect clusters in liquid crystals. These quadrupolar defect clusters, stabilized by the medium's chirality and the tendency to form twisted configurations, are shaped into arbitrary two-dimensional patterns, including reconfigurable phase gratings capable of generating and controlling optical phase singularities in laser beams. Our findings bridge the studies of defects in condensed matter physics and optics and may enable applications in data storage, singular optics, displays, electro-optic devices, diffraction gratings, as well as in both optically- and electrically-addressed pixel-free spatial light modulators.

opological defect lines play a prominent role in many scientific fields[1–15]. For example, optical orbital angular momentum transfer can be enabled by optical vortices, "dark thread" singular lines around which the light's momentum swirls[2–4]. State of the art displays with unprecedented refresh rates and controllable viewing angles[16] are nowadays made of a liquid crystal (LC) in the so-called "blue phase" that contains a periodic three-dimensional (3D) network of defect lines threading through the medium[16–18]. Defects like cosmic strings[14] and vortex lines in electron beams[8] are hard to obtain and study but often can be understood by probing defects in other topologically similar but more easily accessible systems, such as LCs and laser beams[1–5,8,14].

A nematic LC is typically comprised of rod-like molecules that spontaneously orient themselves along a common direction, described by the so-called director $\mathbf{n}$ with nonpolar symmetry ($\mathbf{n} \equiv -\mathbf{n}$), which is the medium's optical axis[1,17,19,20]. Nematic LCs are true anisotropic fluids, which can flow under shear or gravity while maintaining orientational order, although flows, confinement, and various external fields can introduce large-scale spatial changes of this molecular alignment commonly described by the director field $\mathbf{n}(\mathbf{r})$[17]. The fluid nature of LCs - along with the facile response to external fields, surface confinement and temperature changes - often gives rise to various defects, most notably the so-called "disclinations," the defect lines on which orientational order is disrupted and the orientation of LC molecules typically cannot be defined[1,17]. Even the name "nematic" is derived from a Greek word "thread" and refers to ubiquitous defect lines found in these LCs[17]. Disclinations are classified according to their strength s defined as the number of revolutions by 2π that the director makes around the defect core when one circumnavigates the core once[17]. However, typically occurring because of symmetry-breaking isotropic-nematic phase transition or because of flows, these defects annihilate with time and are hard to generate or control in a reliable manner[1,19,20]. The recent progress in optical generation of defects in LCs was so far restricted to the so-called "torons," which are ensembles of point and ring-shaped singularities[21].

In this work, we design a soft matter system with a delicate interplay of the effects of confinement and chirality to obtain twist-stabilized quadrupolar clusters of half-integer disclinations having opposite signs $s = \pm 1/2$ (Fig. 1). These line defects are then shaped into highly controlled computer-generated patterns, including reconfigurable phase gratings capable of inducing and controlling optical phase singularities in laser beams.
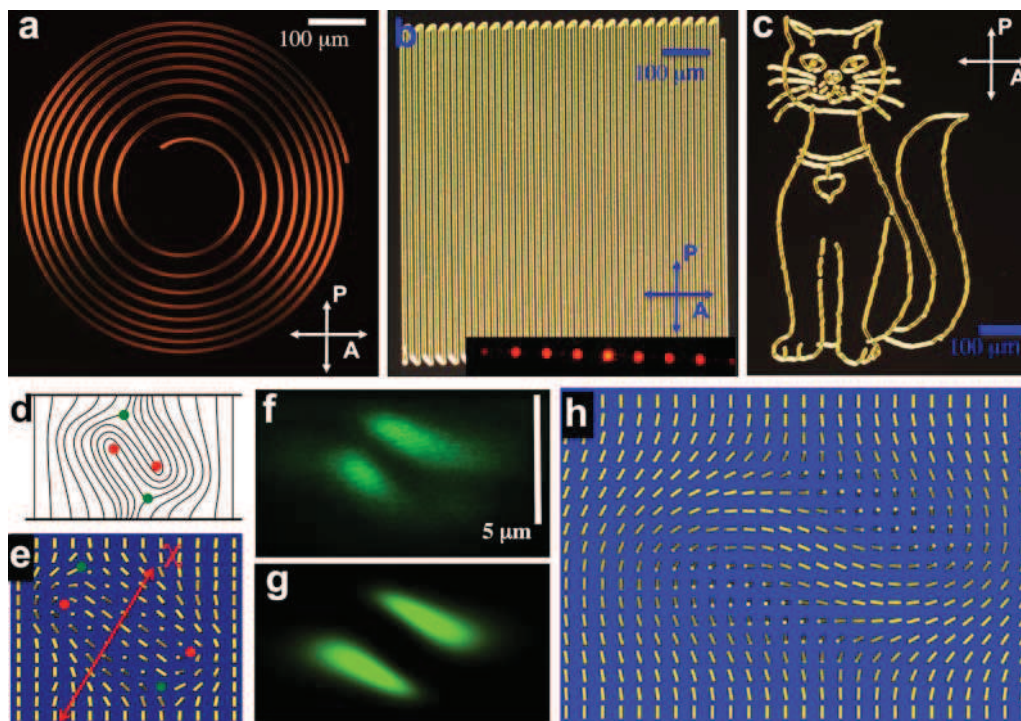
Figure 1 | Laser-generated structures formed by twist-escaped disclination clusters. (a) POM image of a spiral structure. (b) POM image of an optically-generated phase grating composed of the finger structures. The inset shows the corresponding diffraction pattern obtained using a HeNe laser beam. (c) "Topological cat" from the cover of Ref.[9] generated by steering the focused laser beam in the LC cell. (d) (e) Schematics of the director structure with a quadrupole of disclinations of positive and negative half-integer strengths (red and green filled circles, respectively) in (d) a nematic and (e) a cholesteric LC with the qudrupole of the defects running along the finger's length. (f) Experimental and (g) computer-simulated vertical 3PEF-PM cross-sections of the finger's structure in a plane orthogonal to the finger. (h) Computer-simulated director structure in the vertical cross-section of an individual finger. The director fields are visualized by use of cylinders representing rod-like molecules of the LC. "P" and "A" in (a) (b) and (c) mark crossed polarizer and analyzer in POM.

Results

In our study, the nematic LC is doped with a small amount of a chiral agent that promotes formation of twisted configurations of $\mathbf{n(r)}$ with the equilibrium cholesteric pitch p (distance over which the director in a corresponding ground-state structure twists around the helical axis χ by 2π) tuned to be approximately equal to the LC cell thickness d[21–23]. In homeotropic cells with the used p/d ratios within 0.8–1, both uniform and various twisted configurations of $\mathbf{n(r)}$ can exist as stable or metastable states[21–23]. In a sample with initially uniform vertical director field, a focused laser beam locally realigns $\mathbf{n(r)}$ to in-plane orientation, which then promotes formation of self-assembled linear structures directed along the beam scanning direction. These structures are then shaped into desired patterns via continuous steering of the laser beam with intensity above a certain threshold value (Fig. 1a–c), as described in details in the supplementary online material. For example, when using a 10x objective lens of numerical aperture NA=0.25, laser beams of power 0.018 W at the sample plane cause realignment of $\mathbf{n(r)}$ that can be seen as a bright spot in an optical microscope between a set of two crossed polarizers. This threshold power P_{th} is significantly lower than what is needed for the optical realignment in nematic LCs without chiral additives (supplementary material)[21]. Increasing the laser power above a 2nd threshold P_{th2} of about 0.033 W enables a stable generation of the computer-programmed defect structures via scanning of the focused laser beam within the LC sample (Fig. 1a–c) using a laser scanning setup shown in the Supplementary Fig. S1.

Individual $s=\pm1/2$ disclinations are topologically stable entities and cannot appear or terminate in arbitrary locations within a uniformly aligned LC[1]. To make our defect superstructures free of these restrictions, we have utilized the self-assembled quadrupolar clusters

containing half-integer line defects of opposite signs (Fig. 1d,e). In a nematic LC without chiral additives, such defect clusters are unstable because disclinations of opposite signs annihilate each other to minimize bend and splay distortions of $\mathbf{n(r)}$ and the overall free energy due to the defects (Fig. 1d). In the studied chiral nematic LC, however, these defect clusters are stabilized by the energetically favorable twist of $\mathbf{n(r)}$ interspacing disclinations of opposite signs (Fig. 1e). They can also be introduced into the sample in a form of fragments of clusters as the disclinations of opposite sign can annihilate with each other at their ends and can also pin to the confining surfaces (see supplementary information for details). To demonstrate that the defect lines can be optically shaped into arbitrary two-dimensional (2D) architectures, we generate a spiral-shaped structure (Fig. 1a), straight fragments of the defect clusters with sharp turns forming a periodic grating (Fig. 1b), and a sketch of the "topological cat" from the book on category theory (Fig. 1c)[9].

In an LC cell with $p/d\leq1$ and vertical boundary conditions, the sample regions outside of the drawn structures have uniform vertical director and appear black when viewed between crossed polarizers in polarizing optical microscopy (POM). The laser-realigned regions appear bright (Fig. 1a–c and supplementary Fig. S2). A close inspection of generated structures by means of rotating polarizers reveals a combination of effects of birefringence and polarization rotation, indicating the presence of director twist across the cell thickness in these sample regions (Fig. 2). To gain more direct insights into the director structure in the sample's vertical cross-section, we perform label-free 3D imaging by means of three-photon excitation fluorescence polarizing microscopy (3PEF-PM)[24] and measure polarized fluorescence patterns emitted by the LC molecules themselves. An example of an image of the director field in the sample's vertical
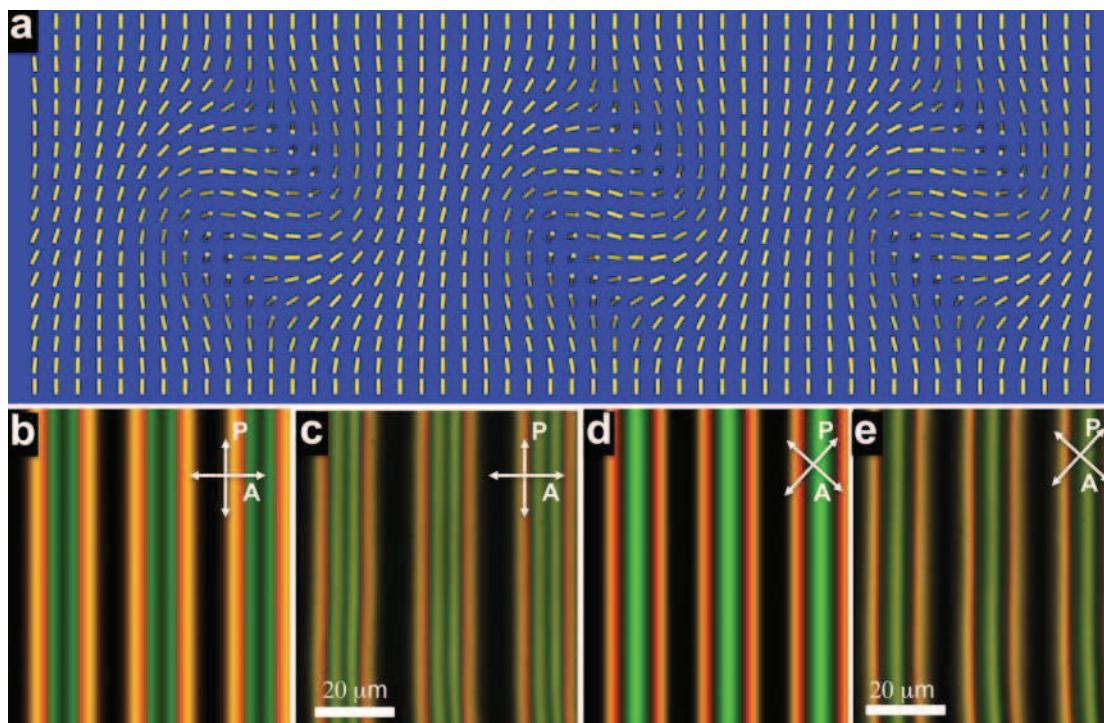
Figure 2 | Director structure and POM images of periodic cholesteric finger arrays. (a) Director field in the vertical cross-section of a periodic finger array. (b) (c) POM textures obtained (b) by means of computer simulations and (c) experimentally for crossed polarizer and analyzer parallel and perpendicular to fingers, respectively. (d) (e) POM textures obtained (d) by means of computer simulations and (e) experimentally for crossed polarizer and analyzer at $\pi/4$ to fingers. Both experimental and computer-simulated POM textures were obtained for $d=p=10$ μm.

cross-section is shown in Fig. 1f, in which fluorescence intensity scales as $\propto \cos^6\phi$, where ϕ is the angle between the spatially varying $\mathbf{n}(\mathbf{r})$ and the linear polarization direction of the excitation laser. Using this and other images obtained for various polarization states and cross-sectional planes (supplementary Figs. S3 and S4), we reconstruct the director structure schematically shown in Fig. 1e (see supplementary information for details). Experimental POM (Fig. 2c,e) and 3PEF-PM textures (Fig. 1f) closely resemble the corresponding computer-simulated textures (Fig. 2b,d and Fig. 1g) obtained for the minimum-energy $\mathbf{n}(\mathbf{r})$ configurations of either a single finger shown in Fig. 1h or a periodic finger array shown in Fig. 2a.

The studied defect clusters consist of a quadrupole of disclinations bound by helicoidal twist occurring predominantly along the direction of a helical axis tilted with respect to the confining substrates. This optically-generated structure resembles that of cholesteric fingers of the first kind previously observed in confined cholesteric cells occurring spontaneously or under applied electric fields[22,23]. Tight tiling of the fingers with defect clusters generated next to each other (Fig. 1b and Fig. 2c,e) typically maintains the tilt of the helical axis and the alignment of the elastic quadrupoles of so-called λ-disclinations (Fig. 2 and supplementary Fig. S2 and S3). Occasionally, the tilting direction of optically drawn fingers can reverse at sharp turns - like the kinks at the edges of the grating shown in Fig. 1b and in an individual finger shown in the supplementary Fig. S4 – while preserving the low-energy nature of cores of λ-disclinations in which melting of the LC is avoided via twisting of the director to become parallel to the defect lines in their center (i.e., the singularities "escape through twist")[17].

Since the effective refractive index of the LC depends on the orientation of $\mathbf{n}(\mathbf{r})$ with respect to the polarization and propagation direction of light, optically generated structures of fingers can be used as tunable and reconfigurable phase diffraction gratings (Fig. 1b). A typical diffraction pattern obtained by means of such a

grating is shown in the inset of Fig. 1b. Computer programmed laser beam scanning provides the capability of unprecedented optical control over the structure of such gratings. Shown in Fig. 3a–c are POM images of optically generated diffraction gratings with edge dislocations (insertions) of different magnitude $b=|\mathbf{b}|=ma$ of Burgers vector, where a is the periodicity of the optically drawn grating and m is the integer number of insertions. The diffraction patterns obtained by use of these phase gratings have one or more dark spots within the beams of 1st and higher diffraction orders (Fig. 3d,e). Characterization of phase profiles of laser beams in different diffraction orders n_{do} using the Stokes Polarimetry method[25] and a setup shown in the supplementary Fig. S5 reveals optical phase singularities and the relation between their topological charge N and b (Fig. 3): $N = \pm b \cdot n_{do}/a$, in agreement with theoretical predictions[26–28], where N is an integer number of 2π phase change on any closed circuit around the singularity center. The details of phase distributions are visualized by means of grayscale representations shown in the bottom parts of Fig. 3f,h and the 3D representations (Fig.3g,i). The phase varies continuously everywhere within the beams except for the locations of the screw dislocations ($=$phase singularities), where phase is undefined. Remarkably, similar to the case of high-charge defects in LCs known to split into defects of lower charge[17], the phase singularities of large N tend to split into multiple phase singularities of elementary charge $N = \pm 1$ (Fig. 3e,h,i). However, the physical origin of this splitting is very different from that of splitting of high-strength disclinations in LCs (driven by minimization of the elastic free energy) and is usually attributed to the presence of a weak coherent background in a screw-dislocated wave[26–28].

Beams with more sophisticated controlled singular phase distributions can be obtained from a Gaussian beam diffracted by phase gratings with multiple edge dislocations. For example, when two spatially separated elementary edge dislocations of opposite Burgers vectors $\mathbf{b}$ are introduced into a periodic grating (Fig. 4a), the intensity profiles of beams in the diffraction pattern shown in Fig. 4b change
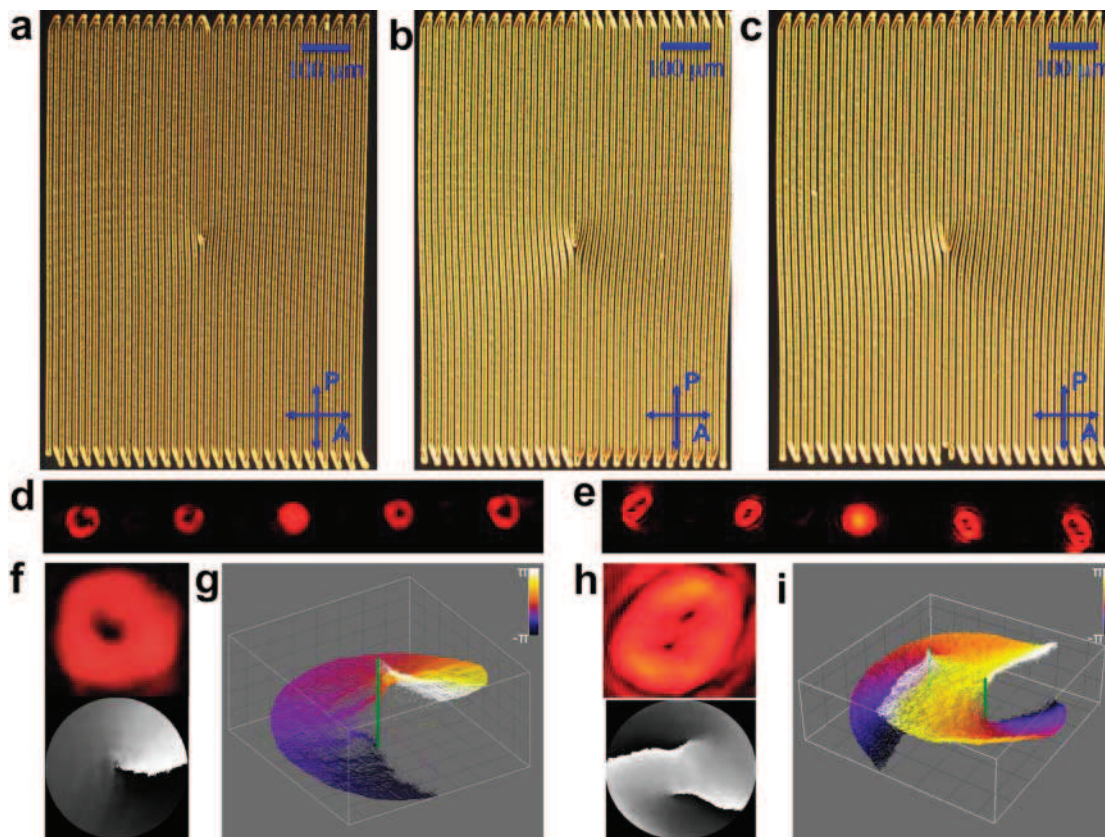
Figure 3 | Diffraction gratings with various dislocations and their use for generation of phase singularities. (a) POM image of a finger grating with an elementary dislocation. (b) (c) POM images of gratings with edge dislocations of larger Burgers vector. (d) Far field diffraction pattern from the grating shown in (a). (e) Far field diffraction pattern from grating shown in (c). (f) Enlarged image of the first-order diffracted beam shown in (d) (top) and its phase profile (bottom) with the phase varying from $-\pi$ (black) to π (white). (g) 3D plot of the phase profile of the beam shown in (d). (h) Enlarged image of the first-order diffracted beam shown in (e) (top) and its phase surface (bottom). (i) 3D plot of the phase profile of the beam shown in (e). The vertical green lines mark the phase singularities.

dramatically as compared to diffraction patterns due to gratings with individual edge dislocations (Fig. 3). The corresponding phase distributions (Fig. 4c) reveal inter-connected screw-edge dislocations: two screw dislocations having elementary charge of opposite signs are connected by an edge dislocation in the phase profile across which the phase has a sharp jump from $-\pi$ to $+\pi$[26–28]. On the other hand, two slightly separated dislocations with the same **b** in a grating shown in the supplementary Fig. S6a produce two off-axis rotating elementary phase singularities of the same sign $N=\pm1$ in the $n_{do}=\pm1$ beams and $2n_{do}$ such defects in the beams of higher order[26]. The angle α between the straight line linking two phase singularities in the first-order beam and the straight line between two edge dislocations in the grating varies with the distance d_c from the phase grating to the camera detector as shown in the supplementary Fig. S6b, according to theoretically predicted dependence (see supplementary material)[26].

Because of the LC's fluid nature and its facile response to electric field, the optically drawn phase gratings can be tuned and fully erased by AC voltages of about 1 V at 1 kHz. As voltage U applied to the transparent indium tin oxide electrodes of the cell continuously increases, the fingers first shrink in width for $U \leq 0.5$ V (Fig. 5a,b) and then shrink in length starting from the edge dislocation core and grating ends (Fig. 5c) until the phase grating is fully erased at $U \approx 5.6$ V (Fig. 5d). The structural changes in fingers and their eventual erasing are due to coupling of $\mathbf{n(r)}$ in the used LC of positive dielectric anisotropy with the low-frequency electric field $\mathbf{E}$ that tends to minimize the electric field term of the free energy by enforcing $\mathbf{n(r)} \| \mathbf{E}$. LC elasticity, on the other hand, resists this realignment as it drives the system away from the global or local minima of the elastic free

energy. At each applied voltage, the observed equilibrated static director structures correspond to the minima of the total free energy (the sum of electric and elastic free energy terms) evaluated for the given vertical surface boundary conditions for $\mathbf{n(r)}$. The field induces structural transformations and ensuing changes in the effective refractive index distribution within the grating. By varying the applied voltage, one can tune the width of fingers and the effective index distribution within them at low voltages (Fig.5a,b) and then fully "erase" them at higher voltages (Fig. 5c,d). This control of the phase gratings enables the corresponding control of the diffraction patterns, as shown in the bottom parts of Fig. 5a–d and in Fig. 5e. Importantly, the left-right asymmetry of the diffraction patterns, which is due to the synclinic tilting of the fingers' structures in the grating, becomes even more pronounced at high voltages and persists until the grating disappears at voltages of 5.6 V and higher (Fig. 5e). Interestingly, as the voltage gradually increases from 0 to 1.4 V, the diffracted beam of first order on the left side first increases and then decrease in intensity while the beam of first order on the right side constantly increases in intensity (Fig. 5e). Both left-side and right-side second-order diffracted beams continuously decrease in intensity and the 0-th order beam continuously increases in intensity. In our experiments, similar voltage tunability was achieved for diffraction patterns with and without dislocation defects as well as for different polarizations of the incident light (e.g. circular and linear parallel, perpendicular and at 45 degrees to the fingers direction). The observed dependence of laser intensity in the diffraction patterns on the polarization of the incident laser beam is due to the fact that the spatially-varying effective refractive index of the uniaxial LC
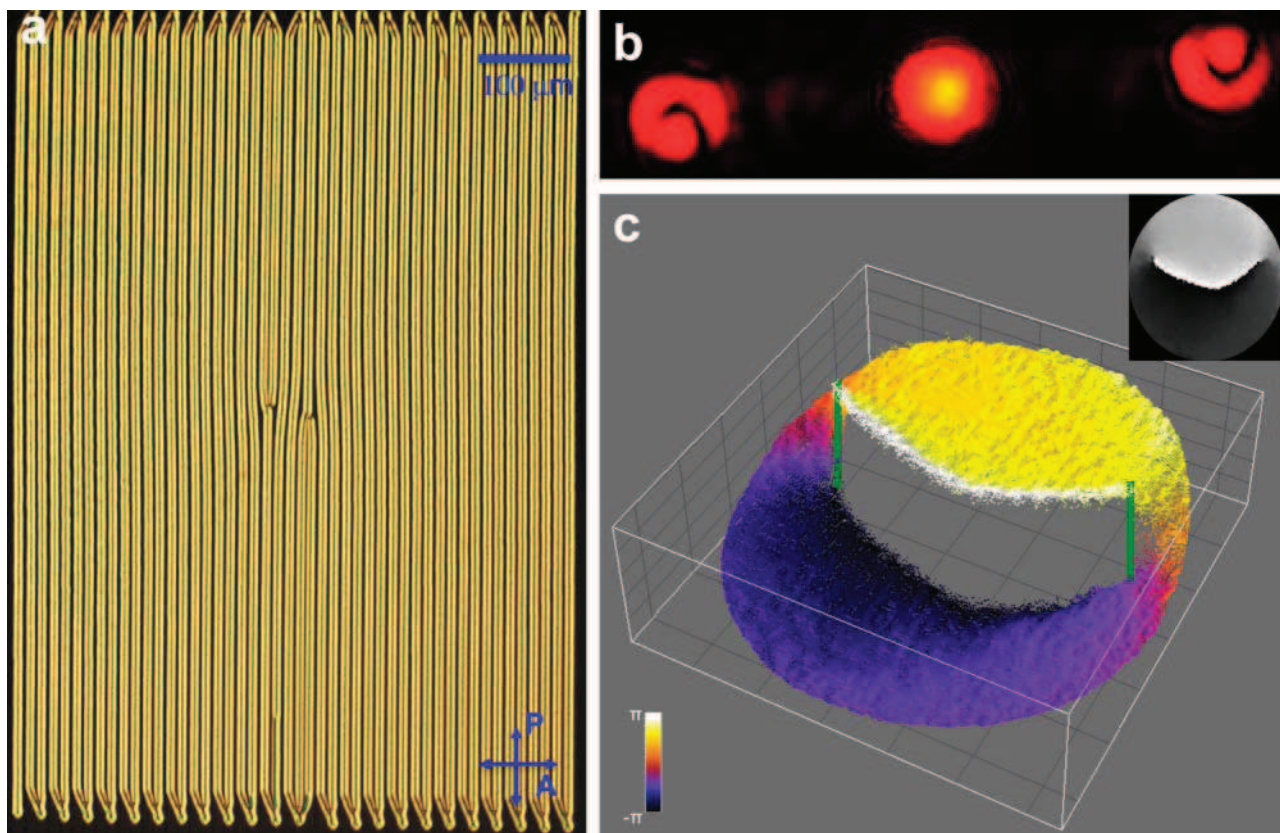
Figure 4 | Generation of phase singularities with interlinked screw-edge dislocations. (a) The POM image of a grating with two slightly separated elementary dislocations of opposite signs of Burgers vector. (b) Corresponding diffraction pattern with only 0th and 1st diffraction orders shown. (c) 3D representation of the phase profile corresponding to the first-order diffraction beam. The inset shows the corresponding 2D representation of the same phase singularity. The vertical green lines mark the screw dislocations.

medium within the periodic grating is strongly dependent on the polarization of this beam. The ability to control intensities of different diffraction orders by varying relatively low applied voltages (0.5–2 V) and also "erasing" these gratings at somewhat higher (∼5 V) is of great interest for a number of important applications of phase diffraction gratings[29–33].

Times needed for optical generation of the fingers structures are typically predetermined by the fastest speed of continuous scanning of a focused laser beam using galvano mirrors that still yields reliable generation of uninterrupted fingers (100 µm/s in the case of using a 10x objective). 2D patterns of fingers can be generated within times ranging from a fraction of a second to minutes, depending on complexity of the pattern. The fingers structures can be unwound at applied voltages of 5 V and higher or modified at lower voltages within a typical response time of 5–10 ms, comparable to the response time of nematic LCs confined into cells of similar thickness[17]. In order to decrease the laser generation times, one can utilize holographic laser tweezers instead of the scanning-beam approach used in our current work[21,29,34], which may potentially shorten these times to ∼10 ms, comparable to the LC's response time.

Discussion

Although conventional electrically addressed LC spatial light modulators (SLMs) have recently emerged as a powerful means for generation of optical phase singularities and control of phase of light on a pixel-by-pixel basis[31], some of their major limitations as compared to microfabricated gratings and masks are caused by relatively large minimum size and limited number of pixels. For example, liquid crystal on silicon SLMs with pixels much smaller than in other LC SLMS, that can be used only in the reflective mode, typically have pixel size within 5–10 µm and larger[31]. Our findings may allow for development of both phase-only and amplitude-only optically and electrically controlled SLMs that overcome these limitations because the generation of finger structures requires no patterned electrodes or complicated electric addressing of pixels and the size of laser-generated structures can be designed to be in the submicrometer range (via selecting appropriate cholesteric pitch and cell thickness). Optically generated gratings therefore combine advantages of conventional gratings and masks that have no pixelation-related problems with the advantages of tunability and switching offered by conventional LC SLMs. Furthermore, our approach may also offer a simple means for microfabrication of thin flexible films with highly controlled diffraction gratings. To do this, by using reactive mesogens instead of small-molecule LCs, one can first generate desired diffraction gratings or other patterns by a scanned infrared laser beam and then polymerize the LC to obtain thin films with imprinted phase gratings or masks for applications in singular and Fourier optics.

Highly controlled periodic arrays of defects are of great interest for the study of interactions between various nanoparticles and topological defects and self-assembly mediated by such interactions[35–41]. It is of interest to explore how individual finger fragments as well as their loops and arrays with and without various defect-entrapped nanoparticles can be potentially utilized as phase masks for generation of nontrivial phase profiles in laser beams and for other applications. For example, localization of metal and semiconductor nanoparticles within disclinations in fingers, similar to that reported for other LC defects[35–39,41], may not only allow for obtaining highly controlled spatial patterns of nanoparticles but also enhance or dramatically change the response of phase gratings and phase masks.
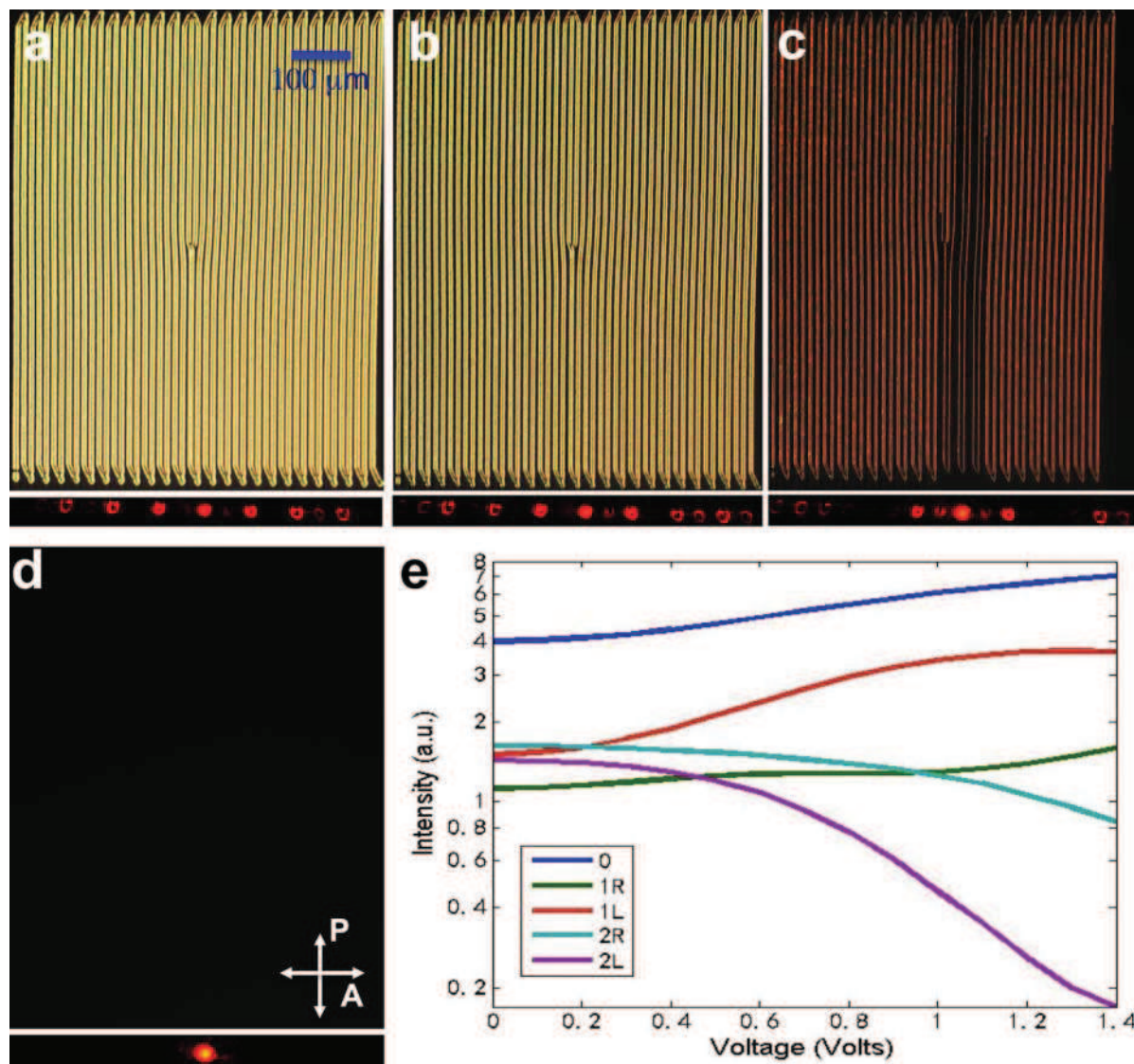
Figure 5 | Voltage control of fingers gratings and the corresponding diffraction patterns. (a)–(d) POM images of a grating with an elementary disloca-tion at applied voltages of (a) 0 V, (b) 1.8 V, (c) 3.6 V, and (d) 5.6 V. The corresponding diffraction patterns are shown in the bottom of figure parts of (a)–(d). (e) intensity of light in different diffraction orders vs. applied voltage. The 1st and 2nd diffraction orders are labeled "1L", "2L", "1R", and "2R" in (e) with "L" and "R" standing for "left" and "right," respectively.

One of the major recent research efforts in soft matter and other branches of condensed matter physics is directed at control of topo-logical defects using fields, colloids, optical tweezers, confinement, chirality, and other means[34–44]. Our findings greatly extend the cur-rent capabilities and possibly also the utility of such control of defects. Furthermore, using laser generated patterns of defects as a model system, one can obtain insights into how defects in condensed matter can be probed based on the study of phase profiles in various types of beams (e.g. electron beams[5,8]) at wavelengths comparable to the size of structural features in material systems of interest.

From the standpoint of view of using laser-generated defect pat-terns as reconfigurable and tunable diffraction gratings, it is inter-esting that the studied diffraction patterns are strongly asymmetric and that the difference between intensities of diffracted beams of different diffraction orders varies as a function of applied voltage (Fig. 5). This phenomenon is likely due to the asymmetric director structure of the finger used to draw the grating (Fig. 1h and Fig. 2a) and the corresponding asymmetric profiles of the phase gratings obtained by tight tiling of fingers while maintaining the directionality of the tilt of the finger's helical axis. A comprehensive experimental

and numerical study of diffraction patterns and diffraction efficien-cies due to gratings composed of fingers will be reported elsewhere.

To conclude, we have demonstrated unprecedented control over hierarchical defect structures spanning from defect lines in the LC director field, to defects in gratings optically generated from such line defects, and to the optical phase singularities obtained by use of such gratings with inserted dislocation defects. This work bridges the study of defects in condensed matter physics and optics and may enable new applications in singular optics, display and diffractive devices, data storage, etc.

Methods

Integrated laser scanning and optical imaging setup. The used laser scanning system consists of a two-axis scanning head XLRB2 (Nuttfield Technology) and a continuous wave Ytterbium-doped fiber laser (1064 nm, from IPG Photonics) with collimated output beam diameter of 5 mm (supplementary Fig. S1). It is designed to steer a focused beam along arbitrary 2D computer-programmed trajectories within the focal plane of a microscope objective. Two scanning mirrors enable voltage-controlled 2D beam deflection and are powered by a digital-analog converter (NI PCI-MIO-16E-4, from National Instruments) controlled by homemade Labview software. The laser beam is first directed into the scanning head, reflected by its two

mirrors, and then introduced into the microscope by means of a telescope (supplementary Fig. S1). The scanning mirror axes are positioned at the front focal plane of the first lens of the telescope, while keeping the distance between the two lenses of the telescope to be the sum of their focal lengths and the back focal plane of the second lens conjugate with the back aperture of the microscope objective.

The laser scanning system is integrated with an upright polarizing optical microscope BX-51 (Olympus). The sample is placed between two crossed polarizers and viewed in a transmission-mode POM while the defect structures are being generated and manipulated via steering the focused beam. Imaging light traversing through the LC regions with vertical $\mathbf{n}(\mathbf{r})$ is blocked by the set of crossed polarizers, since the light's polarization remains unchanged. Cell regions with fingers alter polarization of incoming linearly polarized light due to the horizontal component of $\mathbf{n}(\mathbf{r})$ and its twist, so that POM textures reveal the defects and $\mathbf{n}(\mathbf{r})$. Both structural generation and POM imaging are implemented by use of microscope objectives with 10x–100x magnification and numerical apertures (NA) within NA = 0.1 − 1.4.

Three-photon excitation fluorescence polarizing microscopy. 3D director structures were probed using the 3PEF-PM, which is an imaging modality of the nonlinear optical polarizing microscopy technique described in detail elsewhere[24]. A tunable, pulsed Ti:sapphire oscillator (Coherent Chameleon Ultra-II) is employed as an excitation source for the 3PEF-PM. The oscillator output can be tuned over a 680–1080 nm wavelength range with 140 fs pulse durations at an 80 MHz repetition rate. To control the linear polarization state, the beam is passed through a rotatable half-wave plate and a Glan-Thompson polarizer, and then directed into the scanning head (Olympus FV-300) of an inverted optical microscope IX-81 (Olympus). A 100x objective with high $NA = 1.4$ focuses the beam to a diffraction-limited spot while a pair of galvano mirrors within the scanning head steers the spot within the focal plane of the objective. A stepper motor controls the height of the objective so that 3D images can be reconstructed from a series of two-dimensional scans. Since the excitation intensities needed to induce significant three-photon absorption only exist in a small volume around the focus of the objective, this approach provides an intrinsic submicrometer 3D optical resolution. We use a beam tuned to 870 nm wavelength to excite the LC molecules directly via the three-photon absorption process and detect the emitted fluorescence signal in an epi-detection scheme using a bandpass filter centered at 417 nm (bandwidth 60 nm) and a photomultiplier tube[24]. Since the transition dipole moments of absorption and fluorescence are along the long axes of LC molecules, polarized multiphoton excitation yields orientation-sensitive fluorescence textures with the signal intensity $\propto \cos^6\phi$, where ϕ is the angle between $\mathbf{n}(\mathbf{r})$ and the linear polarization direction of laser excitation light[24]. 3PEF-PM textures obtained for different sample cross-sections and for complementary 3PEF-PM imaging polarizations allow us to reconstruct the 3D $\mathbf{n}(\mathbf{r})$.

Optical phase mapping setup. The used phase mapping technique is based on the measurements of Stokes parameters using a setup shown in the supplementary Fig. S5. A 633 nm He-Ne laser beam of diameter 1 mm is split into two beams of the same intensity by a beam splitter. One of the beams is passed through the phase grating and then the diffracted beams of interest with phase singularities dependent on the diffraction order are selected by a mirror and polarized vertically using a linear polarizer. The reference beam is polarized horizontally. The beam from a studied diffraction order of interest and the reference beam are collimated and recombined. A quarter wave plate and polarizer on the optical train of the recombined beam control the phase delay and polarization as needed to measure different Stokes parameters. A complementary metal–oxide–semiconductor (CMOS) camera Nikon D300 is used to measure the intensity profiles of the laser beams. Four images are obtained for different orientations of the quarter wave plate and the polarizer and then used to reconstruct the phase distribution in different diffraction orders (see supplementary material for details).

Materials and sample preparation. LC cells were constructed using glass substrates with transparent indium tin oxide (ITO) electrodes. To obtain vertical surface boundary conditions for $\mathbf{n}(\mathbf{r})$, we treat the glass plates by dip-coating in a 5 wt.% aqueous solution of a surfactant [3-(trimethoxysilyl)propyl]octadecyl-dimethylammonium chloride (DMOAP). To set the cell gap, ultraviolet-light-curable optical adhesive NOA-61 (from Norland Products Inc.) doped with glass microspheres of diameter matching the desired gap thickness was used to glue the substrates together via ultraviolet light exposure. To obtain chiral nematic LC mixtures of different p, we doped the room-temperature nematic hosts E7, MLC-6815, and ZLI-3412 (all from EM Industries) with different concentrations C of the chiral additive CB15 (EM Industries) according to the relation $p = 1/(C \cdot H_{HTP})$ and using known values of helical twisting power H_{HTP}, which, for example, is $H_{HTP} = 7.3\,\mu m^{-1}$ in the case of E7. Material properties of the used LCs are provided in the supplementary Table S1. All experimental data presented in this work have been obtained for cholesteric LC mixtures based on the E7 nematic host. We infiltrated the cells by use of capillary forces at elevated temperature of about 90°C, sealed them using 5-min epoxy glue, and soldered wires to the ITO electrodes.

Computer simulations of POM textures. Using the computer-simulated 3D director structure of an array of three parallel cholesteric fingers (Fig. 2a), we have simulated the corresponding POM textures (Fig. 2c,e) using the Jones matrix method[31,32] and experimental material parameters such as optical anisotropy, pitch, and cell thickness (supplementary Table S1). The LC sample with a finger was split into a set of thin slabs parallel to substrates with known orientation of $\mathbf{n}(\mathbf{r})$ given by numerical modeling

(supplementary material). While traversing through the LC cell, light splits into ordinary and extraordinary waves with electric fields perpendicular and parallel to the in-plane projection of $\mathbf{n}(\mathbf{r})$, respectively. The effect of each thin slab is equivalent to that of a phase retardation plate with spatially varying optical axis and is described by a coordinate-dependent Jones matrix[31]. In each pixel of a simulated polarizing microscopy texture, intensity of the light after propagation through the cell is obtained by successive multiplication of the Jones matrices corresponding to a polarizer, the series of thin nematic slabs with coordinate-dependent phase retardation, and the analyzer. To mimic the achromatic-light observations in the experiments, we have performed these calculations for wavelength 475 nm, 510 nm, and 650 nm and then superimposed the resulting textures to obtain the POM images. Computer-simulated images closely resemble experimental results, Fig. 2b–e, and further reaffirm our understanding of director configurations based on computer simulations and reconstruction using 3PEF-PM images.

1. Chaikin, P. M. & Lubensky, T. C. *Principles of Condensed Matter Physics* (Cambridge University Press, Cambridge, 2000).
2. Allen, L., Beijersbergen, M. W., Spreeuw, R. J. C. & Woerdman, J. P. Orbital angular momentum of light and the transformation of Laguerre Gaussian laser modes. *Phys. Rev. A* **45**, 8185–8189 (1992).
3. Leach, J., Dennis, M. R., Courtial, J. & Padgett, M. J. Vortex knots in light. *New J. Phys.* **7**, 1–11 (2005).
4. Leach, J., Dennis, M. R., Courtial, J. & Padgett, M. J. Laser beams: knotted threads of darkness. *Nature* **432**, 165 (2004).
5. Uchida, M. & Tonomura, A. Generation of electron beams carrying orbital angular momentum. *Nature* **464**, 737–739 (2010).
6. Muhlbauer, S. *et al.* Skyrmion lattice in a chiral magnet. *Science* **323**, 915–919 (2009).
7. Irvine, W. T. M., Vitelli, V. & Chaikin, P. M. Pleats in crystal on curved surfaces. *Nature* **468**, 947–951 (2010).
8. Verbeeck, J., Tian & Schattschneider, P. Production and application of electron vortex beam. *Nature* **467**, 301–304 (2010).
9. Adamek, J., Herrlich, H. & Strecker, G. E. *Abstract and Concrete Categories-The Joy of Cats.* (Heldermann Verlag Press, 2004).
10. Dennis, M. R., King, R. P., Jack, B., O'Holleran, K. & Padgett, M. J. Isolated optical vortex knots. *Nat. Phys.* **6**, 118–121 (2010).
11. Lopez-Leon, T., Koning, V., Devaiah, K. B. S., Vitelli, V. & Ferandez-Nieves, A. Frustrated nematic order in spherical geometries. *Nat. Phys.* **7**, 391–394 (2011).
12. Alexander, G. P., Chen, B. G., Matsumoto, E. A. & Kamien, R. D. Power of the Poincare group: elucidating the hidden symmetries in focal conic domains. *Phys. Rev. Lett.* **104**, 257802 (2010).
13. Irvine, W. T. M. & Bouwmeester, D. Linked and knotted beams of light. *Nat. Phys.* **4**, 716–720 (2008).
14. Chuang, I., Durrer, R., Turok, N. & Yurke, B. Cosmology in the Laboratory: Defect Dynamics in Liquid Crystals. *Science* **251**, 1336–1342 (1991).
15. Poulin, P., Holger, S., Lubensky, T. C. & Weitz, D. A. Novel colloidal interactions in anisotropic fluids. *Science* **275**, 1770–1773 (1997).
16. Liu, L.-W., Wang, Q.-H. & Cui, J.-P. A continuous-viewing-angle-controllable liquid-crystal display using a blue-phase liquid crystal. *J. of the Society for Information Display* **19**, 547–550 (2011).
17. De Gennes, P. G. & Prost, J. *The Physics of Liquid Crystals* (Oxford University Press, New York, 1995).
18. Coles, H. J. & Pivnenko, M. N. Liquid crystal "blue phases" with a wide temperature range. *Nature* **436**, 997–1000 (2005).
19. van Oosten, C. L., Baastiansen, C. W. M. & Broer, D. J. Printed artificial cilia from liquid-crystal network actuators modularly driven by light. *Nat. Mater.* **8**, 677–682 (2009).
20. Woltman, S. J., Jay, D. G. & Crawford, G. P. Liquid-crystal materials find a new order in biomedical applications. *Nat. Mater.* **6**, 929–938 (2007).
21. Smalyukh, I. I., Lansac, Y., Clark, N. & Trivedi R. Three-dimensional structure and multistable optical switching of triple twist toron quasiparticles in anisotropic fluids. *Nat. Mater.* **9**, 139–145 (2010).
22. Smalyukh, I. I. *et al.* Electric-field-induced nematic-cholesteric transition and three-dimensional director structures in homeotropic cells. *Phys. Rev. E* **72**, 061707 (2005).
23. Oswald, P., Baudry, J. & Pirkl, S. Static and dynamic properties of cholesteric fingers in electric field. *Phys. Reports* **337**, 67–96 (2000).
24. Lee, T., Trivedi, R. P. & Smalyukh, I. I. Multimodal nonlinear optical polarizing microscopy of long-range molecular order in liquid crystal. *Opt. Lett.* **35**, 3447–3449 (2010).
25. Denisenko, V. G., Minovich, A., Desyatnikov, A. S., Krolikowski, W., Soskin, M. S. & Kivshar, Y. S. Mapping phases of singular scalar laser beams. *Opt. Lett.* **33**, 89–91 (2008).
26. Soskin, M. S. & Vasnetsov, M. V. Singular Optics. *Progress in optics* **42**, 219–276 (2001).
27. Basistiy, I. V., Bazhenov, V. Yu., Soskin, M. S. & Vasnetsov, M. V. Optics of light beams with screw dislocations. *Opt. Comm.* **103**, 422–428 (1993).
28. Nye, J. F. & Berry, M. V. Dislocations in wave trains. *Proc. R. Soc. Lond.* A **336**, 165–190 (1974).

29. Trushkevych, O., Ackerman, P. Crossland, W. A. & Smalyukh, I. I. Optically Generated Adaptive Localized Structures in Confined Chiral Liquid Crystals Doped with Fullerene. *Appl. Phys. Lett.* **97**, 201906 (2010).

30. Anderson, J. E., Watson, P. E. & Bos, P. J. *LC3D: Liquid crystal display 3-D director simulator software and technology guide* (Artech House, Boston, 2001).

31. Yeh, P. & Gu, C. *Optics of Liquid Crystal Displays* (John Wiley & Sons, Inc., 1999).

32. Born, M. & Wolf, E. *Principles of Optics.* (Pergamon Press, 1975).

33. Clarke, D. & Grainer, J. F. *Polarized light and optical measurement.* (Pergamon Press, 1971).

34. Smalyukh, I. I., Kaputa, D., Kachynski, A. V., Kuzmin, A. N., Ackerman, P. J., Twombly, C. W., Lee, T., Trivedi, R. P. & Prasad, P. N. Optically generated reconfigurable photonic structures of elastic quasiparticles in frustrated cholesteric liquid crystals. *Opt. Express* **20**, 6870–6880 (2012).

35. Senyuk, B., Evans, J. S., Ackerman, P., Lee, T., Manna, P., Vigderman, L., Zubarev, E. R., van de Lagemaat, J. & Smalyukh, I. I. Shape-dependent oriented trapping of plasmonic nanoparticles by topological defects. *Nano Lett.* **12**, 527–1114 (2012).

36. Zapotocky, M., Ramos, L., Poulin, P., Lubensky, T. C. & Weitz, D. A. Particle-stabilized defect gel in cholesteric liquid crystals. *Science* **283**, 209–212 (1999).

37. Ramos, L., Zapotocky, M., Lubensky, T. C. & Weitz, D. A. Rheology of defect networks in cholesteric liquid crystals. *Phys. Rev. E* **66**, 031711 (2002).

38. Ravnik, M., Alexander, G. P., Yeomans, J. M. & Zumer, S. P. Three-dimensional colloidal crystals in liquid crystalline blue phases. *Procs. Natl. Acad. Sci. USA* **108**, 5188–5193 (2011).

39. Trivedi, R. P., Klevets, I. I., Senyuk, B. I., Lee, T. & Smalyukh, I. I. Multi-scale interactions and three-dimensional patterning of colloidal particles and defects in lamellar soft media. *Procs. Nat. Acad. Sci. U.S.A.* **109**, 4744–4749 (2012).

40. Lapointe, C., Mason, T. & Smalyukh, I. I. Shape-controlled colloidal interactions in nematic liquid crystals. *Science* **326**, 1083–1086 (2009).

41. Skarabot, M., Ravnik, M., Zumer, S., Tkalec, U., Poberaj, I., Babic, D. & Musevic, I. Hierarchical self-assembly of nematic colloidal superstructures. *Phys. Rev. E* **77**, 061706 (2008).

42. Mosseri, R. Geometrical frustration and defects in condensed matter systems. *C. R. Chimie* **11**, 192–197 (2008).

43. Osterman, N., Kotar, J., Terentjev, E. M. & Cicuta, P. Relaxation kinetics of stretched disclination lines in a nematic liquid crystal. *Phys. Rev. E* **81**, 061701 (2010).

44. Wood, T. A., Lintuvuori, J. S., Schofield, A. B., Marenduzzo, D. & Poon, W. C. K. A self-quenched defect glass in a colloid-nematic liquid crystal composite. *Science* **334**, 79–83 (2011).

Acknowledgements

Author contributions

P.J.A. and Z.Q. generated structures and characterized phase singularities. P.J.A. designed and fabricated all studied samples. Y. Lin and Z.Q. wrote the Labview software for laser beam scanning. P.J.A. and C.W.T. did initial proof-of-principle studies on generation of fingers structures and imaging. Y. Lansac computer-simulated director structure of fingers. P.J.A. simulated POM and 3PEF-PM textures. P.J.A., Z.Q., and M.J.L. constructed the setup for optical phase characterization. I.I.S. conceived and planned the project, provided funding, and explained results. P.J.A. and I.I.S. wrote the paper.

Additional information

How to cite this article: Ackerman, P.J. *et al.* Laser-directed hierarchical assembly of liquid crystal defects and control of optical phase singularities. *Sci. Rep.* **2**, 414; DOI:10.1038/srep00414 (2012).

Supplementary online material

Laser-directed hierarchical assembly of liquid crystal defects and control of optical phase singularities

Paul J. Ackerman,[1,2] Zhiyuan Qi,[1] Yiheng Lin,[1] Christopher W. Twombly,[1] Mauricio J. Laviada,[1] Yves Lansac,[1,3] and Ivan I. Smalyukh[1,2,4,5,*]

[1]*Department of Physics and Liquid Crystal Materials Research Center, University of Colorado, Boulder, Colorado 80309, USA. *e-mail: ivan.smalyukh@colorado.edu*

[2]*Department of Electrical, Computer, and Energy Engineering, University of Colorado, Boulder, Colorado 80309, USA*
[3] *GREMAN, Université François Rabelais-CNRS, UMR 7347, 37200 Tours, France*
[4] *Materials Science and Engineering Program, University of Colorado, Boulder, Colorado 80309, USA*
[5]*Renewable and Sustainable Energy Institute, National Renewable Energy Laboratory and University of Colorado, Boulder, Colorado 80309, USA*

1. Laser-induced LC realignment and drawing of defect structures

Laser-induced realignment of LC director is an optical-frequency version of the Freederiksz transition that forms the basis for modern display applications.[1,2] The threshold nature of this effect in an initially uniformly aligned LC cell with strong surface anchoring of the director is a result of the competition between the optical and elastic torques. At optical frequencies dielectric anisotropy $\Delta\varepsilon = \Delta\varepsilon_{of} = n_e^2 - n_o^2$, where n_e and n_o are the extraordinary and ordinary refractive indices at the beam's wavelength, respectively.[1] In a homeotropic cell with the initial uniform alignment of unwound $\mathbf{n(r)}$, a laser-induced director realignment occurs when the electric torque

(tending to reorient the director to be parallel to the electric field $\vec{E}$) overcomes the elastic torque (tending to preserve the initial uniform alignment).[1] When the laser beam's waist w is much larger than the LC cell thickness ($w \gg d$), the threshold electric field of the optical wave and the corresponding laser intensity can be found similarly to the low-frequency case:

$$I_{th} = \frac{\pi^2 K_{33} c n_e^2}{(n_e^2 - n_o^2) n_o d^2} \cdot (1 - 4\rho^2 \frac{K_{22}^2}{K_{33}^2})$$

(s1.1)

where $\rho = d/p$ is the confinement ratio of cell thickness and the equilibrium cholesteric pitch, K_{22} and K_{33} are Frank elastic constants for twist and bend deformations, respectively, and c is the speed of light.[2] The threshold intensity for the director reorientation in the frustrated cholesteric LC is smaller than in the nematic LC case by a factor of $(1 - 4\rho^2 K_{22}^2 / K_{33}^2)$. For $\rho = 0$, Eq. (s1.1) reduces to the well-known expression for the threshold intensity in a homeotropic nematic cell:[2]

$$I_{th\_nematic} = \frac{\pi^2 K_{33} c n_e^2}{(n_e^2 - n_o^2) n_o d^2}$$

(s1.2)

Although $w \approx d$ in most of our experiments, the qualitative behavior $I_{th} \propto \frac{K_{33}}{(n_e^2 - n_o^2)} \cdot (1 - 4 \frac{d^2}{p^2} \frac{K_{22}^2}{K_{33}^2})$ still holds.[2] The initial stages of the director realignment in homeotropic cholesteric cells at laser intensities around I_{th} are qualitatively similar to those in nematic cells. However, the dynamic evolution of $\mathbf{n(r)}$ at higher intensities differs substantially and a broad range of 3D twisted configurations can be formed. Furthermore, above well-defined 2nd threshold laser intensity I_{th2}, one can obtain multistable localized configurations such as fingers and torons that do not disappear upon switching off the beam.[2]

We wrote a Labview-based program for steering of the laser beam along programmed trajectories in the plane of the LC cell by means of the 2D scanning mirror system (supplementary Fig. S1). This allows one to generate diffraction gratings with and without

dislocations shown in Figs. 1b, 3a-c, 4a, 5a and supplementary Figure S2a. We have used the theoretical profiles of the layered structure around dislocations obtained in the framework of nonlinear theory of lamellar media[3] to generate fingers gratings with dislocations. For example, to generate grating patterns with an elementary dislocation (Fig. 3a) and with dislocations having larger Burgers vectors (Fig. 3b,c), we have programmed steering of the laser beam along trajectories obtained using the theoretical expression for the layer displacement derived by Kamien and co-workers.[3] A similar procedure and the superposition of layer displacements due to individual dislocation defects are also used to obtain other phase gratings presented in this work. In some of the gratings, we have used continuous drawing of the gratings and other patterns from a single complex-shaped finger (Figs. 1a,b, 2c,e, 3a-c, 4a, 5a), which requires pinning finger only at its two end points. In the other examples (Fig. 1c and supplementary Fig. S2a), we have composed these 2D patterns of fingers from multiple finger fragments. Isolated short fragments of naturally-occurring or optically generated fingers of the first kind have one pointed and one rounded ends (supplementary Fig. S3). 3D imaging reveals that such structures have bulk point defects in the ends of the fingers located at different depths with respect to the cell midplane (supplementary Fig. S3). These defects can be also pinned to the confining surfaces (supplementary Fig. S4), which greatly enhances stability of the fingers and structures generated from them. These findings are consistent with the results of numerical minimization of elastic free energy discussed below.

2. Numerical modeling of laser-generated fingers structures

We use numerical minimization of free energy to obtain the static equilibrium and metastable configurations of $\mathbf{n}(\mathbf{r})$ in confined LCs.[4,5] The free energy density for a cholesteric LC of pitch p under an external electric field $\vec{E}$ of the laser beam is given by $f_{total} = f_{elastic} + f_{field}$, where

$$f_{elastic} = \frac{K_{11}}{2}(\nabla \cdot \hat{n})^2 + \frac{K_{22}}{2}[\hat{n} \cdot (\nabla \times \hat{n}) \pm \frac{2\pi}{p}]^2 + \frac{K_{33}}{2}[\hat{n} \times (\nabla \times \hat{n})]^2 - K_{24}[\nabla \cdot [\hat{n}(\nabla \cdot \hat{n}) + \hat{n} \times (\nabla \times \hat{n})]]$$

,(s2.1)

$$f_{field} = -\frac{\varepsilon_0 \Delta \varepsilon}{2}(\vec{E} \cdot \hat{n})^2$$

.   (s2.2)

where K_{11}, K_{22}, K_{33}, and K_{24} are elastic constants describing splay, twist, bend and saddle splay deformations, respectively. The saddle-splay K_{24} term is known to play a key role in stabilizing the blue phases formed by a periodic 3D organization of double-twist cylinders.[1] The saddle-splay constant K_{24} is difficult to measure experimentally but it is reasonable to assume that $K_{24} = K_{22}$.[6,7]

Minimization of the free energy to find the equilibrium director field is performed using the so-called "director relaxation method."[4,5] We assume that the fingers are infinitely long, are perfectly aligned along a given direction (x-direction) and are translationally invariant along this direction. It is therefore possible to look for 2D equilibrium or metastable structures formed in the plane (y,z), where the y-direction is perpendicular to the cholesteric fingers and the z-direction is perpendicular to the glass plates, i.e along the sample thickness. Equilibrium 2D-structures of $\mathbf{n}(\mathbf{r})$ have $\delta F / \delta n_i = 0$, where n_i is the projection of the director $\mathbf{n}(\mathbf{r})$ onto the i-axis ($i = 1(x), 2(y), 3(z)$) and $\delta F / \delta n_i$ are the functional derivatives of the Frank free energy per unit

length calculated obtained via integration of free energy density over the area perpendicular to the finger

$$F = \int f_{total} dS \qquad \text{(s2.3)}$$

with S being the cross-sectional (y,z)-plane of the sample. From a numerical point of view, the spatial derivatives of the director are computed using a 4th order finite difference scheme. Periodic boundary conditions are applied along $\hat{y}$ - directions while fixed homeotropic boundary condition are used along $\hat{z}$ -direction (cell normal). At each step Δt, the functional derivatives $\delta F / \delta n_i$ are computed and the resulting elementary displacement δn_i defined as

$$\delta n_i = -\Delta t \frac{\delta F}{\delta n_i} \qquad \text{(s2.4)}$$

is projected onto the surfaces $n^2 = 1$ and is taken into account only if it leads to a decrease in the Frank free energy per unit length F. Otherwise, the increment Δt is decreased. This procedure is repeated until the elementary displacement is smaller than a given value set to 10^{-6}. The discretisation is done on grids (N_y x N_z) with N_z = 35 and N_y varying between 119 and 225 in order to make sure that the minimum-energy $\mathbf{n(r)}$ is indeed a structure localized in space in equilibrium with the surrounding untwisted LC and that the periodic boundary conditions do not introduce artifacts affecting its stability. Using grid spacing such as h_y = h_z = 0.05 μm gives sample thickness d = 1.70 μm. The simulations have been done for material parameters of nematic hosts ZLI-3412 and E7. The above minimization procedure is performed for d/p values ranging from 0.75 to 1.2. The initial condition mostly used through this study is constituted of a homeotropic nematic structure on which a random perturbation of the orientation of the director has been applied.   The final equilibrated 2D structure of an isolated CF is also used to create 2D-

periodic arrays of CFs. An example of the minimized CF array obtained from such an initial condition is displayed in the Supplementary Fig. 2b.

3. Stokes polarimetry method of mapping phase of diffracted laser beams

We employ the Stokes polarimetry method[8] to characterize phase singularities in the studied diffraction patterns. To do this, we use a setup shown in the Supplementary Fig. S5 that allows us to select beams of different diffraction orders and then map their two-dimensional phase profiles by analyzing the corresponding two-dimensional patterns of Stokes parameters which carry polarization, phase, and intensity information.[9-12] Using a beam splitter BS1, we split the HeNe laser beam into two beams that are then polarized in two orthogonal directions by polarizers P1 and P2. We pass one of the beams through the diffraction grating and then select the diffracted beam of the diffraction order of interest using a mirror. The 2nd beam is used for reference. The diffracted beam and the reference beam are recombined using the beam splitter BS2. We then use a quarter-wave plate and a polarizer P3 for the measurement of different Stokes parameters by measuring the corresponding 2D intensity distributions $I(\theta_{\lambda/4}, \theta_P)$ for different orientation angles of the quarter-wave plate $\theta_{\lambda/4}$ and the polarizer θ_P. These intensity profiles are recorded with a Nikon D300 CMOS camera while assuring that there is no overexposure. We follow the method described in Ref.[8] to determine Stokes parameters S_2 and S_3 as $S_2 = I(\pi/4, \pi/4) - I(3\pi/4, 3\pi/4)$ and $S_3 = I(\pi/4, 0) - I(3\pi/4, 0)$ (supplementary Fig. S5). The phase difference is then determined as $\delta = \arctan(S_3/S_2)$ while taking into account the basic limitations of the arctangent function (i.e., π is subtracted from the resulting δ if both S_2 and S_3 are negative and added to δ if S_2 is negative while S_3 is positive or zero; when $S_2=0$, $\delta = \pi/2$ for

S_3>0 and $\delta = -\pi/2$ for S_3<0). We utilize Matlab software to analyze the data and visualize the $\delta(x,y)$ phase profiles of beams in the beam's x-y lateral plane and present results using either the 2D gray-scale or 3D color representations (see e.g. Figs. 3 and 4 and supplementary Fig. S6).

4. Rotation of optical phase singularities

The laser-generated diffraction gratings allow one to produce phase singularities that change (e.g. rotate) along the light propagation direction. Furthermore, multiple screw dislocations in the phase of light allow for a direct observation of the so-called Gouy phase shift[13-18] because it manifests itself in the rotation of singularities around the beam axis (Supplementary Fig. S6). In our experiment aimed to demonstrate this, we have laser-generated phase grating with two spatially separated elementary dislocations of the same sign of Burgers vector (Supplementary Fig. S6a) that produce a diffracted beams with two phase singularities. By moving the camera detector along the light propagation direction, we characterize rotation of optical vortices in the first-order diffracted laser beam (Supplementary Fig. S6b) schematically shown in the Supplementary Fig. S6c. We then fit the experimental data with the expected dependence[16-18]

$$\alpha = \arctan(d_c/d_R) + \alpha_{offset} \qquad (s4.1)$$

where α is the Gouy phase shift angle measured between the line connecting the two optical singularities in the lateral plane of the beam and the line connecting centers of two edge dislocations in the phase grating, d_c is the distance between the camera and the phase grating, d_R is the Rayleigh length of the laser beam, and α_{offset} is an offset angle. The obtained fitting parameters are $d_R = 17.5cm$ and $\alpha_{offset} = 3^o$.

7

Supplementary References

[1] De Gennes, P. G. & Prost, J. *The Physics of Liquid Crystals* (Oxford University Press, New York, 1995).

[2] Smalyukh, I.I., Kaputa, D., Kachynski, A. V., Kuzmin, A. N., Ackerman, P. J., Twombly, C. W., Lee, T., Trivedi, R. P., and Prasad, P. N. Optically generated reconfigurable photonic structures of elastic quasiparticles in frustrated cholesteric liquid crystals. *Opt. Express* **20**, 6870-6880 (2012).

[3] Santangelo, C.D & Kamien.R. D., Bogomol'nyi, Prasad, and Sommerfield Configurations in Smectics, Phys. Rev. Lett. 91 045506 (2003).

[4] Gil, L. & Gilli, J. M. Surprising dynamics of some cholesteric liquid crystal patterns. *Phys. Rev. Lett.* **80,** 5742-5745 (1998).

[5] Anderson, J. E., Watson, P. E. & Bos, P. J. LC3D: Liquid crystal display 3-D director simulator software and technology guide (Artech House, Boston, 2001).

[6] Allender, D.W., Crawford, G.P., and Doane, J. W. Determination of the liquid-crystal surface elastic constant K_{24}. *Phys. Rev. Lett.* **67**, 1442-1445 (1991).

[7] Polak, R.D., Crawford, G.P., Costival, B.C., Doane, J.W. and Zumer, S. Optical determination of the saddle-splay elastic constant K_{24} in nematic liquid crystals. *Phys. Rev. E* **49**, R978 (1994).

[8] Denisenko, V.G., Minovich, A., Desyatnikov, A.S., Krolikowski, W., Soskin, M.S., Kivshar, Y.S. Mapping phases of singular scalar laser beams. *Opt. Lett.* **33**, 89-91 (2008).

[9] Yeh, P. & Gu, C. *Optics of Liquid Crystal Displays* (John Wiley & Sons, Inc., 1999).

[10] Born, M., & Wolf, E. *Principles of Optics*. (Pergamon Press, 1975).

[11] Clarke, D., Grainer, J. F., *Polarized light and optical measurement*. (Pergamon Press, 1971).

12. Sharma. K.K, E. *Optics, Principle and application*. (Academic Press, 2006).

13. Gouy, C. R. Sur une propriete nouvelle des ondes lumineuses. *Acad. Sci. Paris.* **110,** (1890)

14. Feng, S. & Winful, H. G. Physical origin of the Gouy phase shift. *Opt. Lett.* **26** 485-487**, (2001)

15. Hariharan, P. & Robinson, P. A. The Gouy phase shift as a geometrical quantum effect. *J. Mod. Opt.* **43**, 219 (1996)

16. Soskin, M. S., Vasnetsov, M. V., Singular Optics. *Progress in optics* **42**, 219-276 (2001)

17. Basistiy, I. V., Bazhenov, V. Yu., Soskin, M. S. and Vasnetsov, M. V. Optics of light beams with screw dislocations. *Optics Comm*. **103**, 422-428 (1993).

18. Baumann, S.M., Kalb, D.M., MacMillan, L.H., and Galvez, E.J. Propagation dynamics of optical vortices due to Gouy phase. *Opt. Express* **17**, 9818 – 9827 (2009).

Supplementary Table

**Supplementary Table S1. Material parameters of the used LCs.**

| Material/property	K_{11}, pN	K_{22}, pN	K_{33}, pN	$\Delta\varepsilon$	Δn	H_{HTP} of CB-15, μm^{-1}
E7	11.1	7.3	17.1	13.8	0.22	7.3
ZLI-3412	14.1	6.7	15.5	3.4	0.078	6.3
MLC-6815	-	-	-	8.1	0.052	6.5

Supplementary Figures
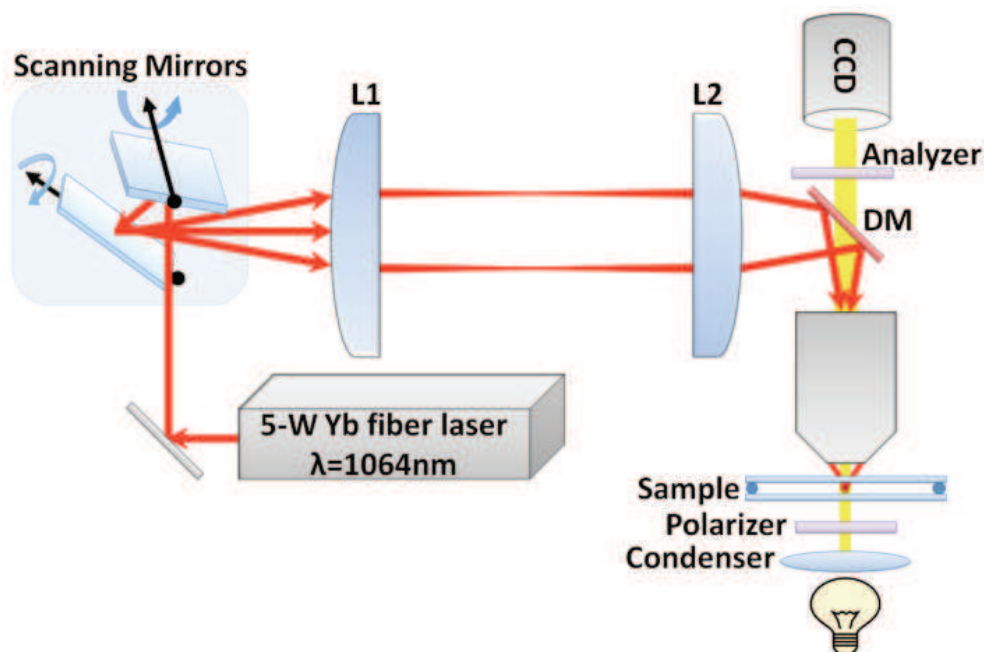
Supplementary Fig. S1. A schematic of a laser manipulation system based on scanning mirrors integrated with a transmission-mode polarizing optical microscope. In the setup, the dichroic mirror is marked "DM" and the two telescope lenses are marked "L1" and "L2".
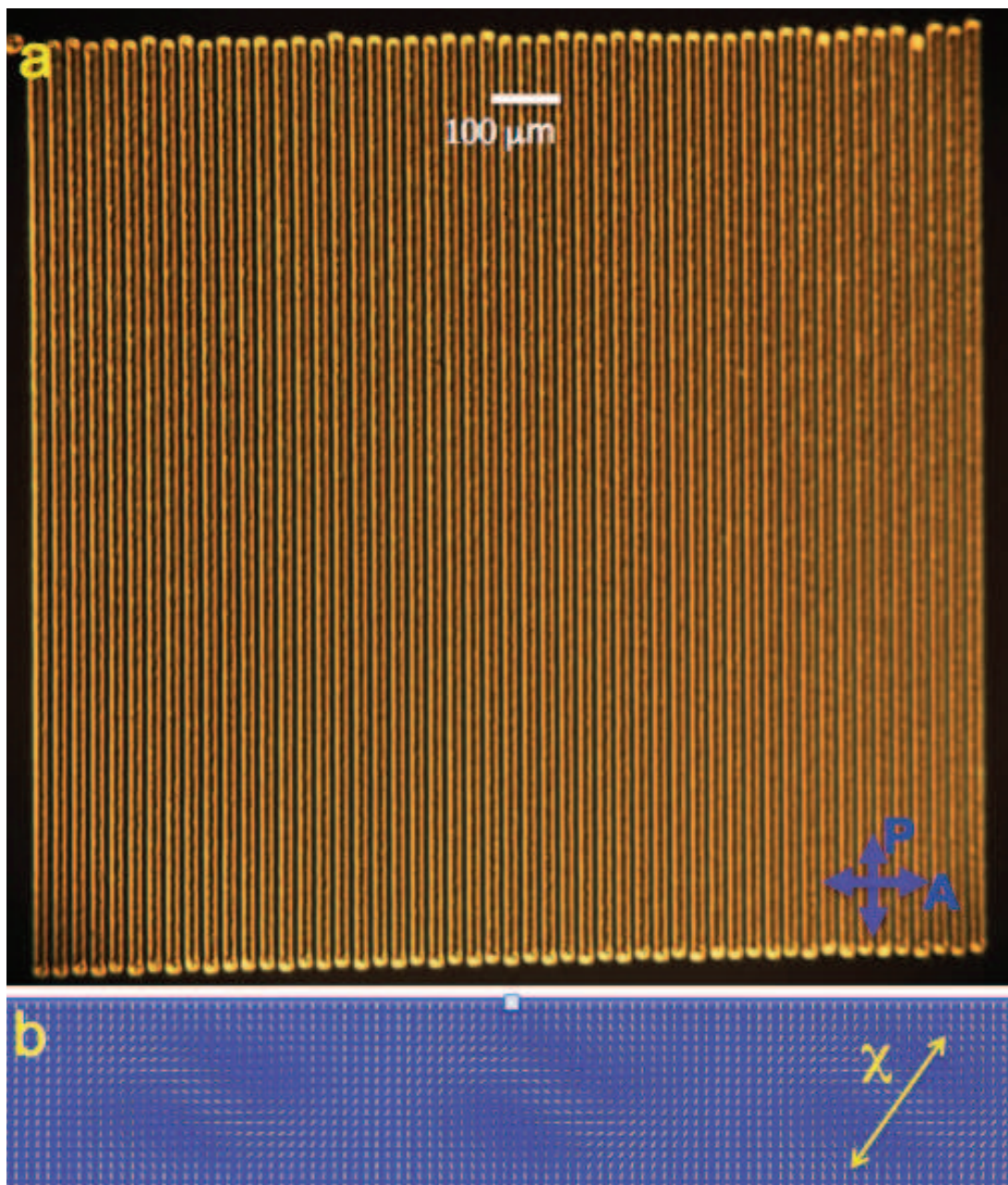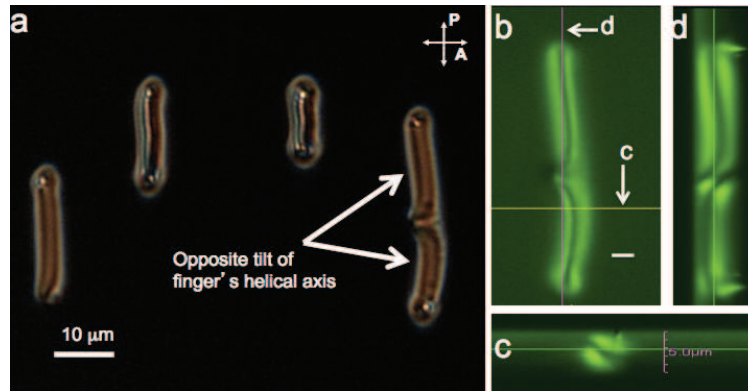
Supplementary Fig. S2. A grating of fingers drawn by scanning the beam in one direction has synclinic tilt of helical axis χ of the neighboring fingers. a, POM image of the grating optically drawn by scanning the laser beam in one direction. **b**, Computer-simulated director structure in the vertical cross-section of such a grating with three fingers next to each other having synclinic tilt of helical axis χ marked with a green double arrow for one of them.
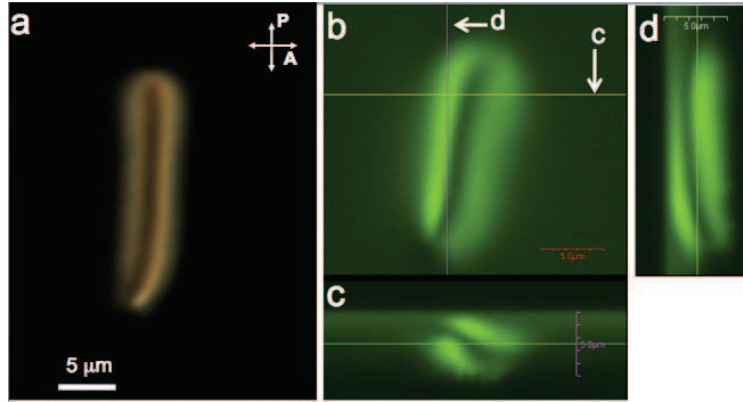
**Supplementary Fig. S3. Finger fragment having one rounded end and one pointed end. a,** POM image between crossed polarizer "P" and analyzer "A" and **b-d,** 3PEF-PM images of the finger. The vertical cross-sections **c,d** labeled in the in-plane 3PEF-PM cross-section shown in **b.** The entire structure and the two ends of the finger are located within the LC bulk.

Supplementary Fig. S4. Pinning of finger ends to confining surfaces. a, POM images of finger fragments having ends within the LC bulk (left) or attached to the confining surfaces (all other fingers). **b-d,** 3PEF-PM images of the finger on the right-side of the POM image shown in **a**. The vertical 3PEF-PM cross-sections **c,d** are labeled in the in-plane cross-section shown in **b**. The vertical cross-section **d**, along the finger length clearly shows that finger ends are pinned to one of the confining surfaces. The white bar in **c**, is 5 μm. Note that the direction of the tilt of the two parts of a finger fragment shown in **b**, is reversed at the point defect in the center.

12
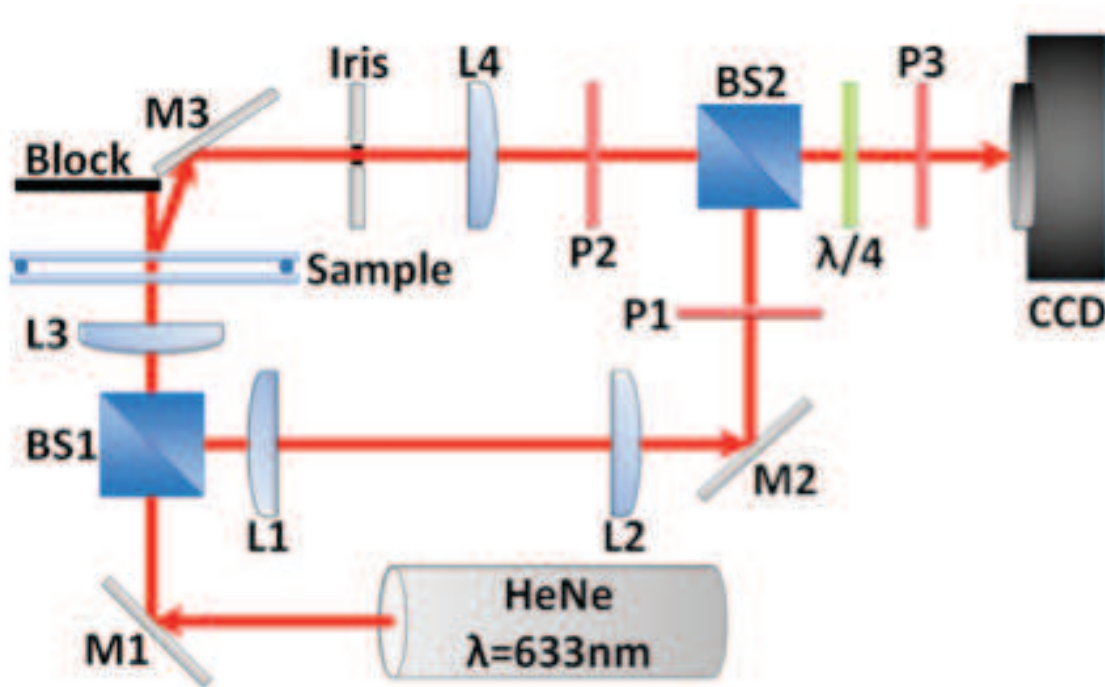
Supplementary Fig. S5. A schematic of the Stokes polarimetry setup used to map the phase of diffracted laser beams. A HeNe laser beam is split into two paths and then recombined by beam splitters BS1 and BS2, respectively. The Block and Iris are used to select the diffraction order of interest. Mirrors M1-M3 are silver mirrors used to redirect the beam. The collimation of beams is performed by lens pairs L1-L2 and L3-L4. Polarizers P1-P3 and the $\lambda/4$ plate control polarization states.
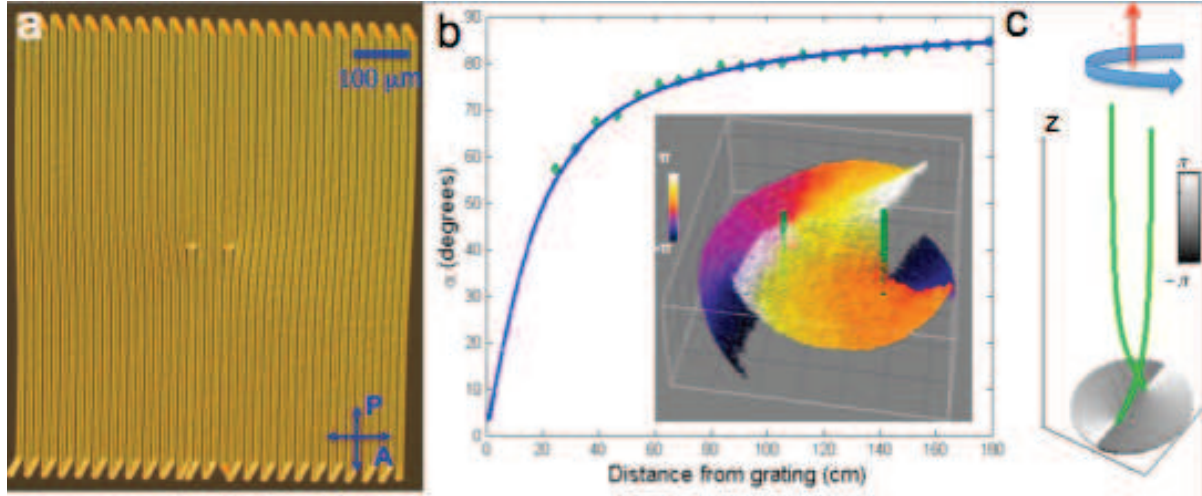
Supplementary Fig. S6. Twisting screw dislocations in the phase of a diffracted beam induced by defects in a finger phase grating. **a**, POM image of finger phase grating with elementary dislocations separated by several finger layers. **b,** Experimental dependence of the angle between singularities in one of the diffracted beams vs. distance d_c (diamonds) and the best fit by the theoretical prediction (solid line). The inset shows the corresponding phase profile of the first-order diffracted beam. **c**, A schematic showing two twisting screw dislocations in the phase of the first-order diffraction beam. The vertical green lines mark the phase singularities.